Observation of magnon polarons in van-der-Waals itinerant ferromagnet Fe_3GeTe_2

Qili Li[1,*,†], Namrata Bansal[1,*], Paul Nufer[1], Lichuan Zhang[2,3], Amir-Abbas Haghighirad[4], Christoph Sürgers[1], Yuriy Mokrousov[3,5], and Wulf Wulfhekel[1,4]

[1]Physikalisches Institut, Karlsruhe Institute of Technology, Karlsruhe, Germany
[2]School of Physics and Electronic Engineering, Jiangsu University, Zhenjiang, China
[3]Peter Grünberg Institut (PGI-1) and Institute for Advanced Simulation (IAS-1) Forschungszentrum Jülich GmbH, Jülich, Germany
[4]Institute for Quantum Materials and Technologies, Karlsruhe Institute of Technology, Karlsruhe, Germany
[5]Institute of Physics, Johannes Gutenberg-University Mainz, Mainz, Germany
[*]These authors contributed equally to this work.
[†]Corresponding author: qili.li@kit.edu

Abstract

Magnon polarons, hybrid quasiparticles embodying the intrinsic coupling between spin and lattice dynamics, bridge magnetism and phononics in quantum materials. Despite extensive studies in magnetic insulators, direct spectroscopic evidence for magnon polarons has been scarcely reported in metallic ferromagnets. Here, we reveal magnon polarons at the nanoscale in single crystals of Fe_3GeTe_2 using inelastic scanning tunneling spectroscopy (ISTS) with a milli-Kelvin scanning tunneling microscope. While ISTS of phonons or magnons has been widely explored, our study focuses on two-dimensional van der Waals (vdW) itinerant ferromagnets, where momentum selection rules normally hinder magnon excitation. We show that strong magnon-phonon interaction leads to hybridization between the magnonic and phononic bands, lifting the selection rules at their avoided band crossings. This emergent momentum selection due to magnon-phonon coupling is a hallmark of magnon polarons. Our findings establish a platform for probing and engineering magnon-phonon hybrid excitations in two-dimensional materials at the nanoscale.

Introduction

The neoteric exploration of two-dimensional (2D) van der Waals (vdW) magnets has recently extended the philosophy of magnonics and spintronics into the 2D realm [1–10]. There, due to their 2D nature, the elementary bosonic excitations in the form of magnons and phonons inherit the strong symmetry breaking of the 2D material, such as anisotropic dispersion [11–15] and chirality [16, 17]. In magnetic 2D materials, the large uniaxial anisotropy and magnetic properties are extremely sensitive to strain engineering [18–23] owing to the low symmetry with strong crystal fields caused by the local surroundings. This potentially leads to an unusually high dynamic coupling between magnetic and lattice degrees of freedom in two dimensions, with strong impact on dynamical properties of 2D magnets. However, to date, very little is known about the nature and properties of elementary magnetic and lattice excitations in 2D magnetic materials. This necessitates the exploration of such excitations, both theoretically and experimentally with various techniques, among which inelastic scanning tunneling spectroscopy (ISTS) emerges as a powerful method [24–30]. ISTS allows us to probe inelastic excitations in structurally-complex 2D materials locally [31]. By now, ISTS has developed into a well established technique to locally resolve vibrons in adsorbed molecules [32], but also has the potential to resolve bulk phonons [29, 30] mostly in materials with strong electron-phonon coupling, i.e. superconductors, surface phonons in noble metals [33–35], and phonons in 2D materials like graphene [36, 37]. Furthermore, ISTS has also been used for the detection of magnons [24–28].

Among 2D magnets [1, 4–10], Fe_3GeTe_2 (FGT) fascinates with its high ferromagnetic transition temperature of 150-220 K in bulk [38–40], even reaching room temperature with gate tuning [41], and metallic traits [38, 39] suitable for STM investigation [42–46]. This prolific material serves as a playground for investigating magnetic skyrmion bubbles [43, 45, 47–50], spin spirals [51], magnetic domains with sharp domain walls [45, 46, 49, 50, 52], large uniaxial anisotropies [38–40, 53–55] and various prominent magnetic properties in 2D world [16, 53, 55–58]. Furthermore, FGT is predicted to show strong magnetoelastic coupling [18], and spin-optical phonon coupling has been investigated by Raman spectroscopy [59–61]. However, it is still elusive for ISTS to detect itinerant ferromagnets with strong magnon-phonon coupling. While magnon polarons have been reported in magnetic insulators, like YIG [62], Cr_2O_3 [63], and 2D $FePS_3$ [64–67] via inelastic neutron scattering, spin Seebeck effect or Raman spectroscopy, it is rarely studied in metallic ferromagnets. This makes FGT an ideal system to study magnon polarons due to magnons, phonons and their interactions by ISTS.

Here we report the nanoscale observation of magnon polarons in the 2D ferromagnetic vdW material Fe_3GeTe_2 (FGT) detected by laterally resolved and spin-polarized ISTS measurements executed with scanning tunneling microscopy (STM) under ultrahigh vacuum and low temperatures (40 mK). Supported by density functional theory and model calculations, we identify the quasi-particle excitations in ISTS of FGT as fingerprints of hybrid magnon-phonon modes (i.e. magnon polarons), which emerge at the crossing points between the magnonic and phononic bands. At these points of strong hybridization, the selection rules for magnon and phonon excitation are softened. This emergent momentum selection largely enhances the scattering cross section with electrons. Our findings provide a platform for investigating and designing the properties of magnon polarons in two-dimensional materials at the nanoscale.

Principles of ISTS

In general, ISTS provides information on the scattering cross section of hot carriers with bosonic excitation in the samples. Within ISTS, inelastic excitations show up most clearly in the form of peak-dip pairs in the second derivative of the tunneling current w.r.t. the bias voltage, symmetrically located in bias voltage around the Fermi level [68]. Vibrons or phonons are created by Coulomb scattering of the hot carriers with the core electrons of the atoms and thus the cross section does not depend on the spin of the tunneling electron and is typically only of the order of few percent. In a 2D sample, the hot carriers injected by the tip thus need to relax by an energy ΔE closer to the Fermi energy by exciting a phonon with energy $\hbar\omega = \Delta E$. As the 2D sample is translational invariant with respect to translation in the 2D plane, the in-plane wave vector $k_\parallel$ is a conserved quantity. In the scattering process, the change of wave vector of the electron thus corresponds to the wave vector of the excited phonon. As phonon creation does not involve the spin of the electron, inelastic transitions comprise of transition between electronic states of the same spin. At low phonon energies, especially for acoustic phonons, inelastic scattering is not prevented by phase space arguments. Arbitrarily small energy transitions are allowed between states of arbitrarily small difference in $k_{\|}$ on the same band (see Fig. 1). Thus, one can expect to observe low-energy phonons in ISTS, but with a relatively weak electron-phonon scattering cross section due to the scattering mechanism. In case of magnons, however, the scattering cross section is significantly larger as the excitation of magnons is driven by the exchange interaction of the tunneling electrons with the spin-polarized sample electrons [25, 69–71]. In phase space, the excitations of magnons are coupled to electronic transitions between bands of opposite spin character. This, however, opens a Stoner gap in the spectrum, as for small energies, the transitions typically do not have a small difference in wave vector (cf. Fig. 1). This suppresses electron-magnon scattering at low energies. An interesting question remains open: what happens to ISTS if there is magnon-phonon coupling?

When taking into account the coupling of phonons and magnons, these selection rules for inelastic electron scattering are lifted at crossing points of the phonon and magnon dispersion. At these points, a hybridization between phonon and magnon modes leading to magnon-polarons is expected, and both the strong exchange interaction and the core scattering can excite the hybrid boson. This effect should show up in the ISTS spectra as distinct peaks at very specific energies given by the dispersion of magnons and phonons.

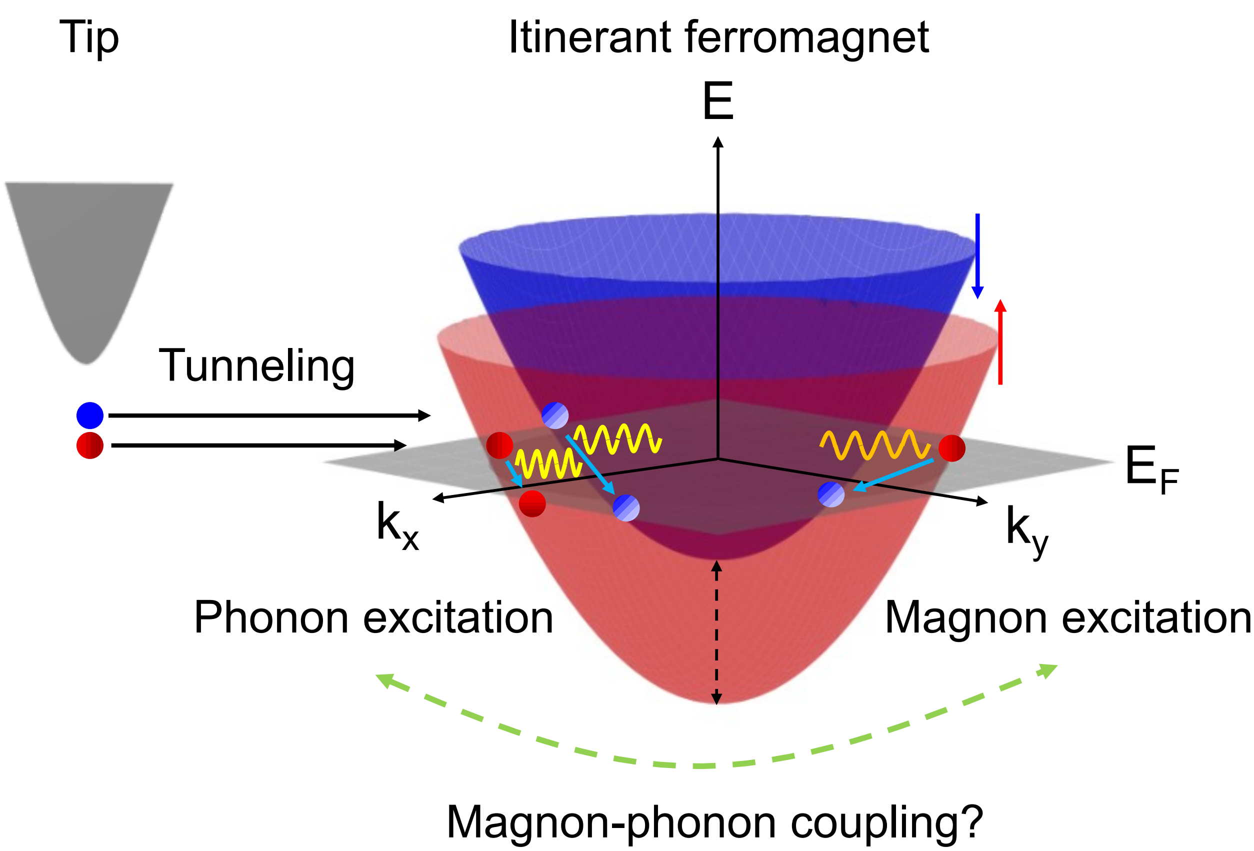

Fig. 1: Sketch of magnon and phonon excitations in an itinerant ferromagnet. Phonon excitation (yellow wavy line) is non-spin-flip process, while magnon excitation (orange wavy line) requires spin flip. Red (blue) indicates spin up (down). The dashed black arrow indicates the exchange splitting (or Stoner gap). A question remains: what will happen if there is magnon-phonon coupling?

Results

Quasiparticle excitations

In FGT, it is widely reported that there is a broad dip in the differential conductivity dI/dU near the Fermi energy (E_F) [42, 45, 46], as depicted in the inset of Fig. 2b. The dip has been interpreted by Zhang *et al.* as a Kondo resonance [42, 72], which is disputed in the literature [45, 46], as the sample is a ferromagnet with relatively large exchange splitting of the electronic bands [18]. For the Kondo effect to appear, the system needs to obey time-reversal symmetry, which is broken in the ferromagnetic ground state. Instead, the exchange interaction of localized spins should split the Kondo resonance by an energy of the order of the exchange interaction. Moreover, the spectroscopic feature manifests as a dip rather than a peak. Although such a dip could in principle be rationalized by interference effects within the Kondo framework [73], a growing body of evidence indicates that many of these Kondo-like dips observed on magnetic adatoms on non-magnetic surfaces are, in fact, signatures of inelastic spinon–polaron (spinaron) excitations [74–76]. A second explanation for the dip in dI/dU could be a dip in the electronic density of states (DOS). DFT calculations for the DOS of FGT, however, exclude this [45]. A third explanation is the disorder-induced electron-electron interaction [77]. However, our samples have low impurity density (inset of Fig. 2a). A fourth possibility for the dip is magnetic inelastic excitations, which we investigate in the following [78–81].

In elastic tunneling, the differential conductance dI/dU is proportional to the DOS of the electrodes [82]. When variations in DOS are negligible on a small energy range around E_F, dI/dU is constant and d^2I/dU^2 vanishes. An additional tunneling channel opens when the kinetic energy of the tunneling electrons is sufficient to cause an inelastic excitation. As the two channels do not interfere, an increment in the current is observed for both signs of the bias voltage. Consequently, steps appear in dI/dU at the brink of the excitation energy $E_g = |eU|$, or equivalently peaks and dips appear in d^2I/dU^2 at $|eU| = E_g$. Fig. 2b shows the differential conductivity in a small interval around E_F recorded at 40 mK with a small lock-in modulation voltage amplitude U_{mod}=500 μV (root mean square $U^{rms}_{\mathrm{mod}} = U_{\mathrm{mod}}/\sqrt{2}$). U_{mod} was chosen as a compromise of energy resolution and signal-to-noise ratio. Clearly, the spectrum deviates from that of a Kondo resonance as steps at various energies can be resolved. In agreement with this, the d^2I/dU^2 spectra, recorded simultaneously with the dI/dU spectra, show five clearly resolved peak-dip pairs symmetrically positioned with respect to E_F, cf. Fig. 2b. Hence, the data in Fig. 2a and Fig. 2b are clear evidence for the occurrence of inelastic tunneling events.

At this low-energy scale of the peaks of 0.3, 0.8, 2.5, 3.8 and 5.2 meV (see arrows), inelastic excitation can be due to either phonons or magnons near the $\overline{\Gamma}$ point, while plasmons, with eV energy, can be excluded. However, note that the individual pairs of peaks and dips are not identical in intensity. Typically, vibron or phonon excitations are rather symmetric in intensity. For magnons, strong asymmetries have been reported due to spin selection rules [25]. To create a magnon by inelastic exchange scattering, either a minority electron needs to be injected into the ferromagnet, or a majority electron needs to be removed. Thus, the asymmetry in intensity of magnon excitation peaks relates to the spin polarization of the magnetic sample, in the case an unpolarized tip is used. The calculated asymmetry, i.e. the difference in the peak area for negative and positive bias divided by their sum, taken from the data shown in Fig.2b, is about -0.1, which is comparable to a DFT value for spin-polarization of the states of about -0.36 at the Fermi energy [45]. Moreover, the peaks ≥ 0.8 (meV) shift with magnetic field (see Supplementary Fig. 1). This proves a magnetic origin of these excitations in FGT. The peak at 0.3 meV remains unchanged under an applied magnetic field. In particular, it consistently appears at very low temperatures in many samples

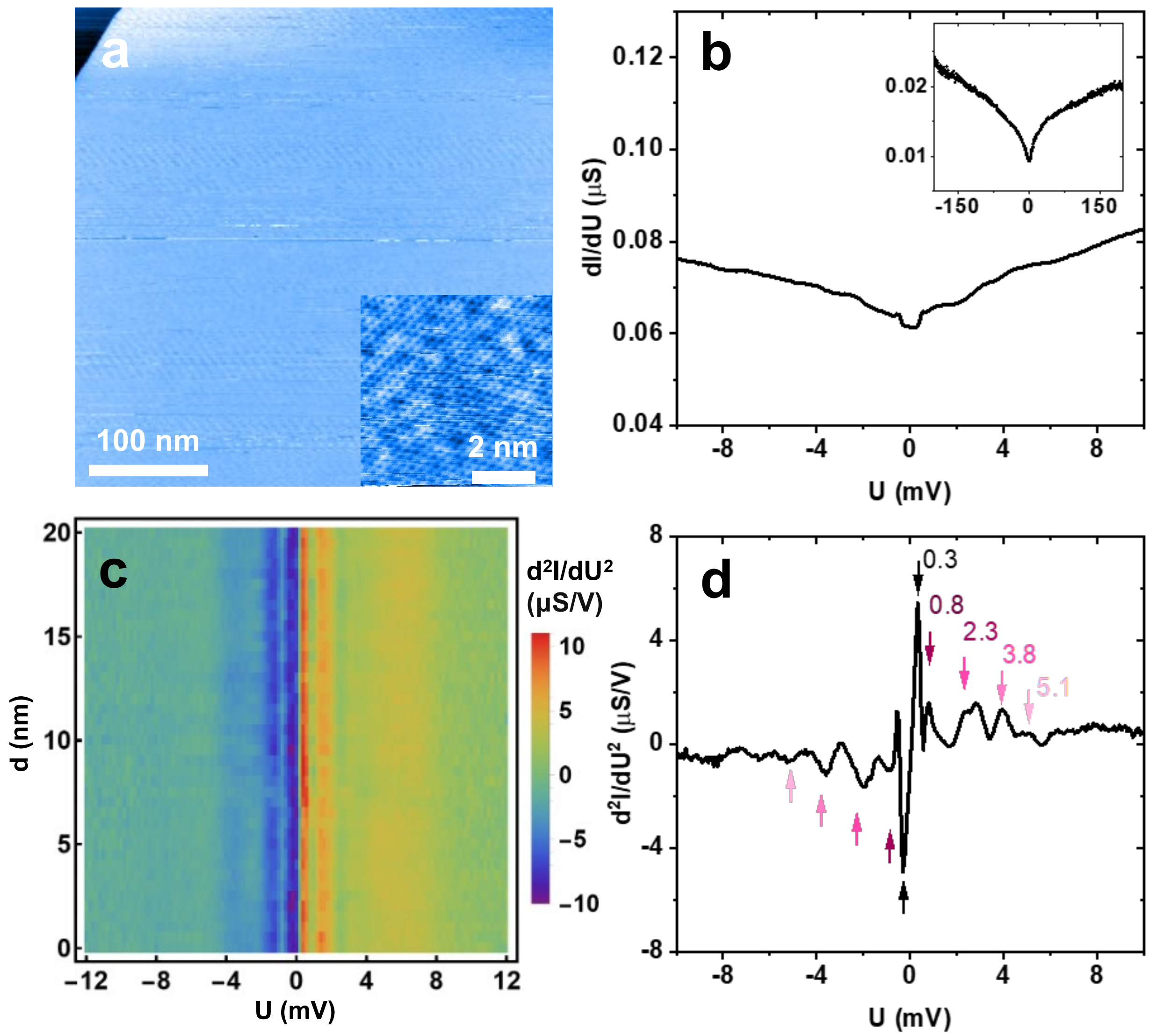

Fig. 2: Low energy excitations via ISTS. a Topography of FGT surface. Inset shows the hexagonal lattice, which is the uppermost Te atoms. **b** dI/dU spectrum averaged over 121 individual curves in a 4×4 nm^2 area. The spectra were measured with W tip at 40 mK (feedback conditions $U = 20$ mV, $I = 2$ nA, $U_{\text{mod}} = 0.5$ mV at 3.421 kHz), and inset figure in **b** was measured with $U = 50$ mV, $I = 1$ nA and $U_{\text{mod}} = 3$ mV at 3.611 kHz. **c** ISTS spectra recorded along a line of 20 nm. ($U = 20$ mV, $I = 5$ nA modulation amplitude $U_{\text{mod}} = 0.5$ mV at 3.611 kHz). **d** d^2I/dU^2 spectra recorded simultaneously in **b**.

and has been attributed to a dynamic Coulomb blockade effect [29, 83–85]. This effect comes from the diverging lifetimes of quasiparticles in Fermi liquids near the Fermi energy and at low temperatures, hindering a second low-energy electron to tunnel into the same state until the first is not scattered. It has also been seen on noble metals at low temperatures [85] and manifests itself as a dip at zero bias in dI/dU of a width of about twice $U_{\rm mod}^{rms}$ or as a peak dip feature in d^2I/dU^2 at $\approx \pm U_{\rm mod}^{rms}$. Note that a higher temperature will smear and broaden these peak-dip pairs into one broadened peak (see Supplementary Fig. 2). Similarly, a larger modulation voltage also results in a rather broad peak-dip pairs at energies around 6 meV and beyond. However, in this work, we intend to focus on the sharp inelastic peaks and dips of low energy.

Spin-polarized results

To further confirm the magnetic origin of these excitations, ISTS with spin-polarized tip was employed. In this technique, the STM tip is spin-polarized, such that the tunneling magneto resistance effect (TMR) [86] arises, providing spin-resolved information on the sample. To polarize the tip, $\approx$ 50 ML Cr was deposited on freshly prepared W tips, followed by gentle annealing [87]. The use of antiferromagnetic tips minimizes the magnetic stray field, which exerts a negligible influence on the magnetization of the FGT sample [45]. This allows us to compare inelastic tunneling spectra for the relative parallel and antiparallel orientation of the magnetization of the electrodes, which is the standard test for magnetic excitations [24, 88].

In the following, we compare the ISTS spectra recorded along lines using unpolarized W tips and Cr-coated tips with out-of-plane spin polarization [45]. In Fig. 3b we show the position-dependent inelastic tunneling signal of the structure similar to Fig. 2. The spectra do not vary as expected for a homogeneous sample and a spin-integrating measurement. In contrast, Fig. 3b, recorded with a spin-polarized tip, clearly shows an abrupt lateral variation in the inelastic signal, which coincides with a 180° magnetic domain wall in SP-STM dI/dU map [Fig. 3a]. Thus, on opposite sides of the domain wall, the relative orientation between the tip and sample magnetization changes by 180° and the relative role of minority and majority carriers in the sample are exchanged. The dashed rectangle indicated the domain wall. Figure 3c shows the d^2I/dU^2 map of this transition for representative peaks at 5 mV and 10 mV. There is an obvious transition at 5 mV (upper panel), while this transition is not observed at 10 mV (lower panel). Figure 3d shows the difference of d^2I/dU^2 for different domains in Fig. 3b. At the peak and dip energies seen in the inelastic spectra, we observe an intensity change at the domain wall due to spin-polarized tunneling, which is in agreement with the spin selection rules [25]. In detail, stronger peaks at positive bias (redder colors) coincide with weaker dips at the same but negative bias (greener color) on each of the domains reflecting the spin selection rules. When crossing the domain wall, stronger peaks (and dips) turn to weaker peaks (and dips) corresponding exchanging the role of minority and majority carriers with respect to the tip spin polarization.

This identifies the peaks as magnetic excitations (or magnons) but does not provide an insight into their energetics. Note that the parabolic dispersion of magnons around the zone center does not produce a peaked DOS, and magnons usually result in a rather smooth ISTS signal around the Fermi energy. The calculation of the DOS based on the three-dimensional parabolic dispersions around the Brillouin zone center predicts a DOS proportional to the square root of magnon energy without any peaks in the low-energy range, see Fig. 4a and Methods. Moreover, at low energies, magnon excitation in the 2D vdW material FGT is expected to be suppressed due to the exchange splitting of the bands, i.e. the Stoner gap.

Phonons might lead to sharp van-Hove singularities in the meV range, as ab-initio calculations of the phonon DOS, shown in Fig. 4a in blue, indicate. There are peaks between 10 and 15 meV,

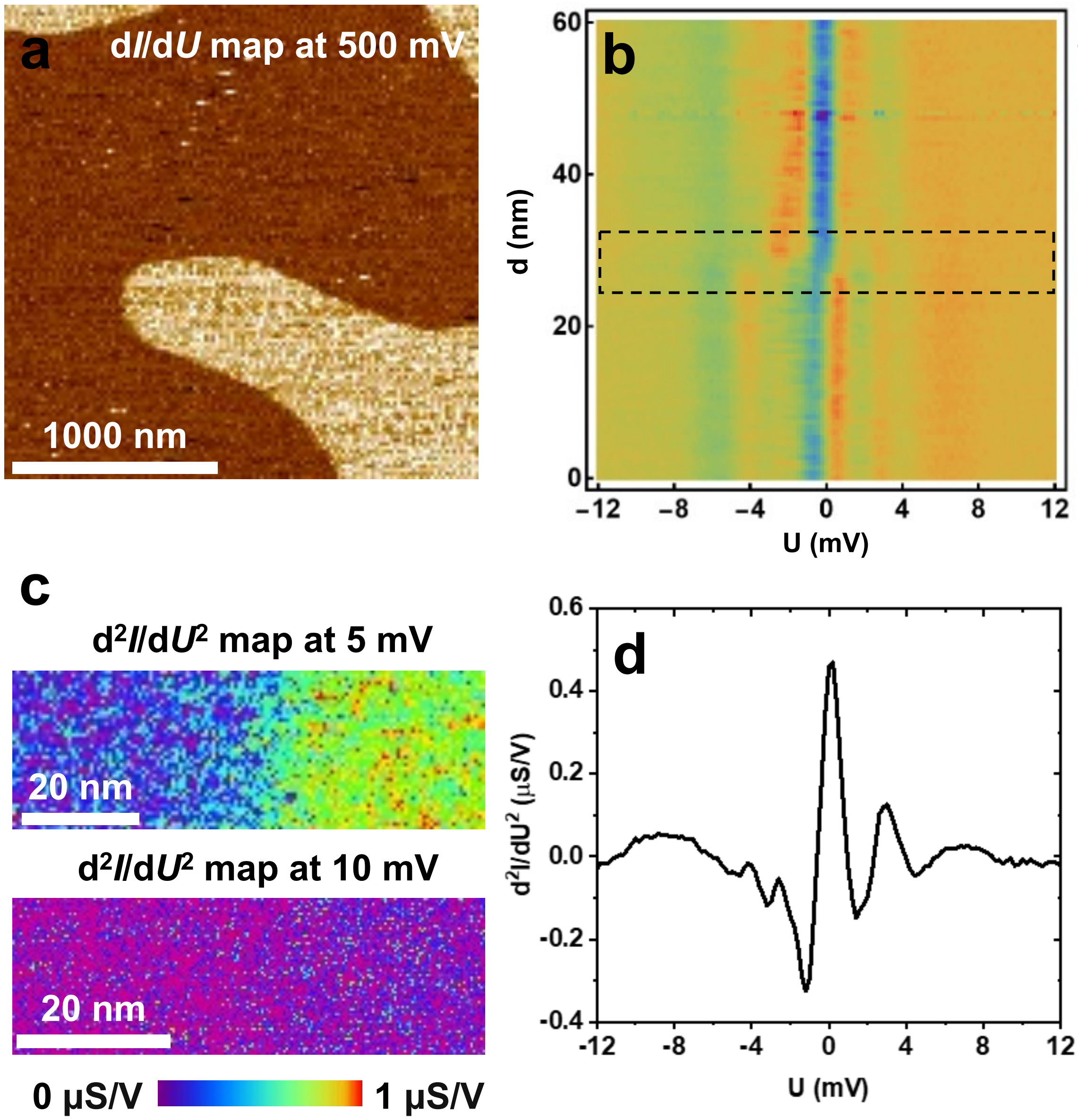

Fig. 3: Spin-polarized results. **a** dI/dU map at 500 mV with Cr-coated W tip (tunneling condition $U = 500$ mV, $I = 0.1$ nA, and $U_{\mathrm{mod}} = 100$ mV). **b** SP-ISTS spectra across a magnetic domain wall ($U = 20$ mV, $I = 0.3$ nA, and $U_{\mathrm{mod}} =1$ mV). The dashed rectangle indicates the domain wall. **c** d^2I/dU^2 maps at 5 mV (upper panel $U = 5$ mV, $I = 0.2$ nA, and $U_{\mathrm{mod}} = 2$ mV at 3.611 kHz), and at 10 mV (lower panel $U = 10$ mV, $I = 0.3$ nA, and $U_{\mathrm{mod}} = 2$ mV at 3.611 kHz). **d** The difference of d^2I/dU^2 for different domains in **b**.

which are consistent with the results of inelastic neutron scattering [14, 15]. Note that we did not observe these phonon peaks in the ISTS shown in Fig. 2. This implies a weak electron-phonon coupling in agreement with recent estimates of only a small electron-phonon coupling constant [89]. Below 5 meV, the phonon DOS is smooth as the lowest energy bands for transversal and longitudinal acoustic phonons disperse linearly in this energy range. When allowing for magnon-phonon coupling, however, the situation drastically changes, as described in the introduction. In case of a

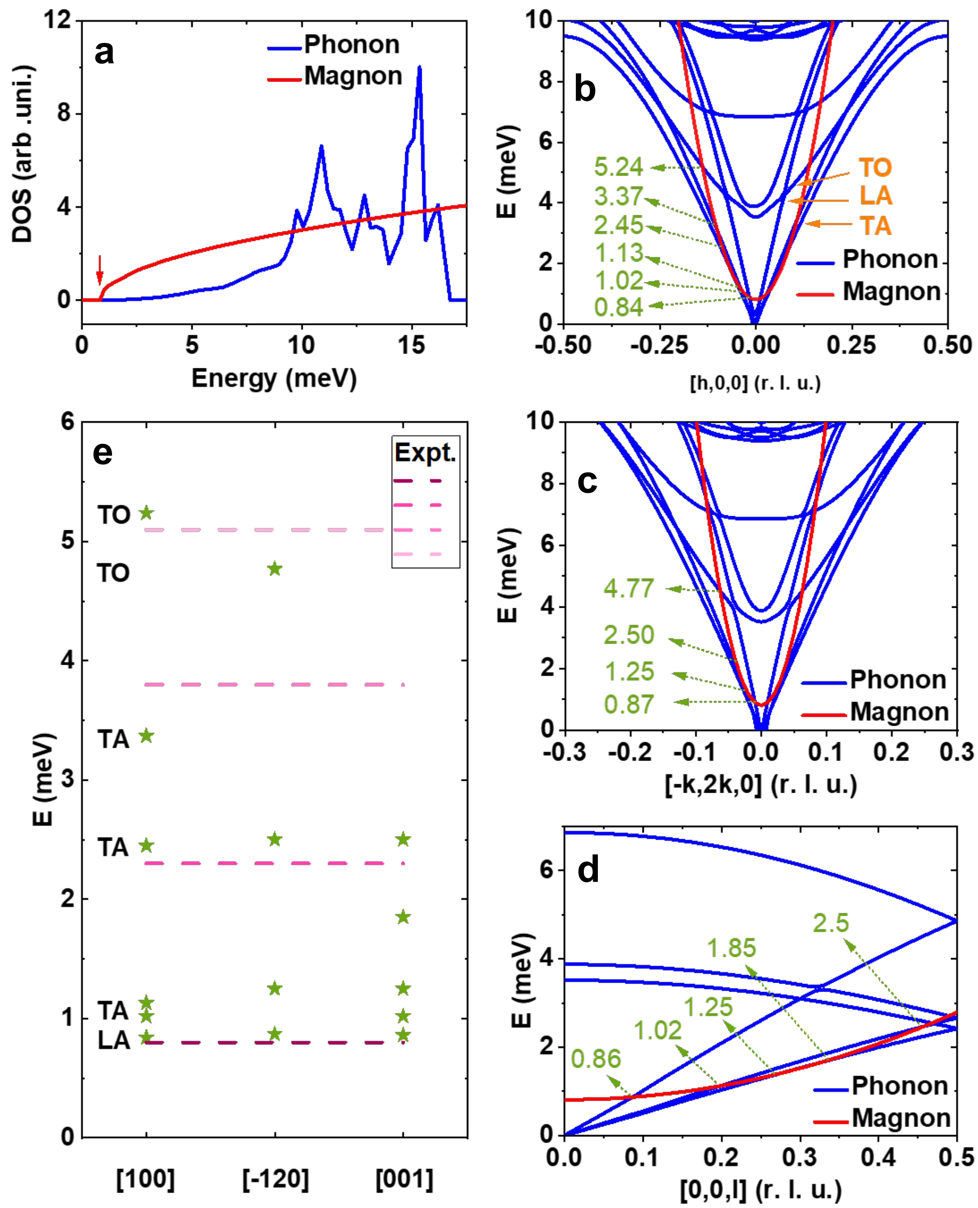

Fig. 4: Magnon and phonon band crossings in FGT. **a** Magnon and phonon DOS in FGT. The phonon DOS is calculated from DFT. The magnon DOS is calculated from three-dimensional, anisotropic and parabolic dispersions around the Brillouin zone center. The red arrow indicates the spin-wave magnon gap (0.81 meV) for our samples. **b** Band crossings between magnon and phonon bands along [100] in reciprocal lattice unit (r.l.u.). The transverse acoustic (TA), longitudinal acoustic (LA), and transverse optical (TO) phonon modes are indicated by the orange arrows. **c** Crossings between magnon and phonon bands along [$\bar{1}$20]. **d** Crossings between magnon and phonon bands along [001]. The spin-wave stiffness for [100], [$\bar{1}$20], and [001] are 69.0 meVÅ^2, 56.7 meVÅ^2, and 53.6 meVÅ^2 from Ref. [14]. **e** Magnon-phonon band crossings compared with d^2I/dU^2 peaks.

crossing between the phonon and magnon bands, magnetoelastic coupling ($H_{me} = \sum_{ij} B_{ij}\epsilon_{ij}S_iS_j$, with B_{ij} the magnetoelastic coupling constants, ϵ_{ij} the strain tensor, and S_i the spin component [90]) hybridizes the two distinct modes and an avoided level crossing is expected. At these so-called "hot spots" in the Brillouin zone, magnetization strongly couples to the lattice, which is also responsible for parts of Gilbert damping [91].

Magnon and phonon band crossings

We suggest that in FGT such avoided level crossings with diabolic points cause a strong coupling of electrons to the hybrid magnon polarons. In Fig. 4b we plot the *ab-initio* phonon dispersion of FGT together with an experimental dispersion curve of the magnons obtained from neutron scattering [14]. The measured spin-wave stiffness from neutron scattering is about 69.0 meVÅ^2 along the [100]-direction, whereas the calculated spin-wave gap is 0.81 meV for our samples (see Methods). Thus, the plot does not contain the fitting parameters see Supplementary Fig. 3 for identifying the band crossings. The plot predicts band crossings of the acoustic phonons – with their linear dispersion – with the parabolic but gaped magnon spectrum very close to the $\overline{\Gamma}$-point at 0.9 meV along all directions in agreement with the observed peak and dip in the inelastic spectrum (see Fig. 4(c,d)). As the quadratic magnon dispersion rises eventually faster, more crossings may appear along the different directions. Note that the magnon dispersion is anisotropic and in the [001]-direction, i.e. normal to the vdW layers, the exchange is weak so that a second crossing with all except the lowest phonon band can be excluded (see Fig. 4d). Figure 4e shows magnon-phonon band crossings compared with d^2I/dU^2 peaks. Along the high-symmetry [100]-direction, second crossings are expected at 2.3, 3.6 and 5.1 meV in excellent agreement with the experimental observations. Crossings along the lower symmetry [$\overline{1}$20]-direction are expected to have a lower spectral weight, and the corresponding peaks are not clearly resolved, or no hybridization occurs in these directions. The theoretically predicted crossing points are in very good agreement with the position of the experimental inelastic peaks and dips shown in Fig. 2d, which clearly demonstrates for the first time the presence of strong magnon-phonon coupling in one of the most prolific 2D materials. Note that there are no crossings below the spin wave gap 0.81 meV. It's consistent with the origin of dynamical Coulomb blockade for the peak at 0.3 meV. Interestingly, optical phonons also cross the magnon dispersion at higher energies, where neutron scattering data shows that the magnon dispersion becomes heavily damped [13–15]. At these energies, no sharp van-Hove singularities are expected, but magnon-phonon coupling for optical phonons has been detected using Raman spectroscopy [59, 61].

Model calculations for magnon polaron excitations

To explain our experimental results, we develop a theory of ISTS for magnon-polaron excited by tunneling electrons (see Methods), which is beyond the usual ISTS widely applied for phonons and magnons. In ISTS, bosons are excited by tunneling electrons, which is distinct from inelatisc neutron scattering [92] and Raman spectroscopy [93], as the electrons themselves deliver the magnetism. This calls for a quantum field description of the problem. The electrons in a material cannot be seen as naked particles, but get dressed by their coupling to bosons. For electrons coupled to phonons, this has been well described by Engelsberg and Schrieffer [94]. The Green's function of the dressed electron is given by the Green's function of the bare electron with its poles in the imaginary part at energies and momenta that correspond to the electron dispersion that becomes lifetime broadened and obtains side bands or kinks due to the phonon energies and momenta [94]. These are the self-energy corrections of the coupled system. Thus, the inelastic tunneling of bare electrons can be regarded as equivalent to elastic tunneling of phonon-dressed electrons.

In summary, ISTS can be understood equivalently as an inelastic scattering process mediated by electron–boson interactions or as an elastic process involving phonon- or boson-dressed electrons.

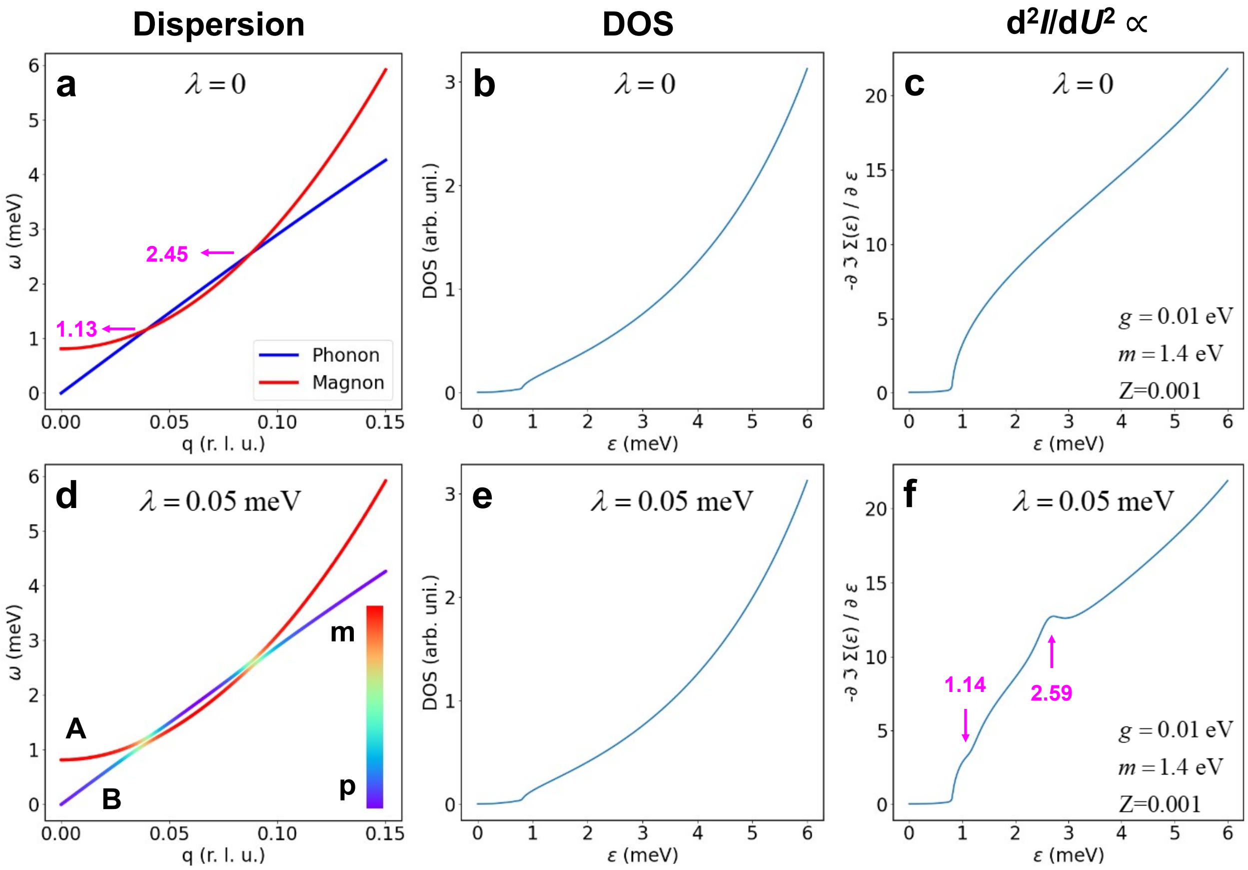

Fig. 5: Model calculations with and without magnon-phonon coupling. **a** Band crossings for magnon and phonon dispersions without magnon-phonon coupling. **b** The corresponding DOS for bosons. **c** The derivative of electron self-energy i.e., ISTS for magnon polaron. **d** Avoided band crossings for magnon and phonon dispersions with magnon-phonon coupling. **e** The corresponding DOS for magnon polarons. **f** The derivative of electron self-energy i.e., ISTS for magnon polaron.

Figure 5a shows the dispersion of the uncoupled bosons and their crossing points, and b shows the sum of their DOS. While the phonons have no gap at the zone center, the magnons display the usual gap due to magnetic anisotropy. Figure 5c shows the negative derivative of electron self-energy. Figure 5d show the dispersion when switching on the magnon-phonon coupling due to magnetoelasticity. An avoided level crossing evolves and the two dispersions hybridize at their crossing. This, however, does not influence the DOS of the bosons (Fig. 5). This in turn means that the observed peaks in the inelastic tunneling spectra cannot be caused by the DOS effect of the hybridized system. At the avoided level crossing, the magnon polaron can be excited in all possible scattering channels. As a consequence, the inelastic scattering cross section should be enhanced at the crossing 5d. A clear peak evolves at the energy of the crossing. Outside the peak, inelastic scattering is possible only for phonons, as magnon excitation is prohibited by the Stoner gap. Figure 5f shows the negative derivative of electron self-energy. Indeed, peaks are presented at the energy of crossings. For the optical phonon case, see Supplementary Fig. 4.

As shown in Methods, the derivative of the electron self-energy is proportional to ISTS, which represents our experimental measurements. The conclusion is that each magnon polaron (or band crossing) will manifest as a peak in the derivative of electron self-energy, namely a peak in ISTS. Note that generally the acoustic phonon bands have two band crossings with magnon band (Fig. 5), while optical phonon bands have one crossings with magnon band (Supplementary Fig. 4).

Discussion

We demonstrate the first nanoscale observation of magnon polarons in metallic ferromagnet FGT, using ISTS. These hybrid excitations emerge near the Brillouin-zone center at the crossings of magnon and phonon dispersions, as supported by both first-principles and model calculations. The coupling of these hybrid excitations to the conduction electrons is particularly strong in two dimensional systems and the suggested mechanism should be present in any magnetic vdW material, as long as the phonon and magnon dispersion cross. Spin-polarized measurements confirm the magnetic character of the observed excitations, and the inelastic signal further reveals variations related to the magnetic domain wall. Owing to the inherently local nature of ISTS, it provides a powerful platform for probing confined collective modes in structured samples.

Our findings open venues not only for magnon-phonon engineering, but also for exploring fundamental spin-lattice phenomena.

Magnon-phonon interconversion: Owing to magnon-phonon coupling, phonons can be used to magnetically excite the system at avoided level crossings. Ultimately, the hybrid bosonic excitations can lead to a chiral nature of the phonons part with the possibility to guide transport of the angular momentum of the lattice. One can envisage that strain engineering could be employed to spatially localize magnons in bulk or even monolayer FGT, enabling magnon waveguides, or inversely, that magnetic domain walls can be used to confine phonons.

Magnon-polaron damping: Due to the additional electronic degree of freedom inherent to itinerant ferromagnets, we can expect a significant damping of meV magnon polarons near the band crossings. The magnon polarons can decay both into phonons, magnons or Stoner pairs of conduction electrons near the hot spots in the dispersion. Consequently, this effect should be experimentally observable in reduced lifetimes of phonons or magnons and change of electric resistivity (Supplementary Information 5 [42, 95]) in the energy and momentum range of the crossings.

Angular momentum dynamics by magnon polarons: The formation of magnon polarons has previously been discussed in terms of spin angular momentum conservation. However, all three participants of the inelastic process – phonons, magnons and electrons – naturally exhibit orbital magnetism in addition to spin. The processes and corresponding experimental manifestations of spin and orbital angular momentum transfer, conservation, and dynamics among the three degrees of freedom at the hybridization points should be explored in the future. Finally, the hybrid bosonic excitations can lead to a chiral nature of the phonons part with the possibility to guide transport of the angular momentum of the lattice.

Methods

Experimental details

High-quality single crystals $Fe_{3-x}GeTe_2$ ($x \approx 0.04$) with Curie temperature $T_C \approx 205$ K (see Supplementary Fig. 5 for resistivity and ref. [45] for magnetic susceptibility of our samples) were cleaved *in-situ* at a base pressure of $p < 1 \times 10^{-10}$ mbar, leading to atomically flat surfaces with only very few step edges separated on the micrometer scale [Fig. 2(a)]. STM measurements were carried out using a home-built low-temperature (40 mK base temperature) dilution STM system [96].

Bandstructure and DOS of phonons

To treat the effect of phonons, we calculate their DOS and dispersion in FGT from *ab initio* using the Vienna *ab initio* simulation package (VASP) [97] within the local density approximation (LDA) [98] for the exchange correlation potential. The projector-augmented wave (PAW) method [99] is used to describe the interaction between the electrons and the nuclei, and 600 eV was selected for the cutoff kinetic energy of the plane wave expansion. The energy convergence threshold was chosen as 10^{-9} eV and the Brillouin zone (BZ) was sampled with a 15×15×5 Γ-centered Monkhorst-Pack grid [100]. The shape and volume of each cell were fully optimized and the maximum force in each atom was less than 0.001eV/Å. The dispersion of phonons was calculated with the code PHONOPY [101, 102] in a 3×3×2 supercell with finite displacement method.

Dispersion and DOS of magnons

The strong unidirectional magnetic anisotropy in Fe_3GeTe_2 results in a spin-wave gap. The spin-wave gap was obtained by Kittel's formula $E_g = g\mu_B(2K_u/M_s - \mu_0 M_s)$ [103–105]. Here, $K_u = 1.46 \times 10^6$ J/m is the unidirectional magnetic anisotropy, and $M_s = 3.9 \times 10^5$ A/m is the saturation magnetization for our samples [45]. Thus, the spin-wave gap obtained is 0.81 meV. We note that a smaller spin-wave gap around 0.5 meV measured by inelastic neutron scattering is due to the Fe inefficiency in their sample $Fe_{2.72}GeTe_2$ [14], which also results in a lower T_C=160 K [14, 106]. However, spin-wave stiffness does not show an obvious dependence on Fe concentration [106]. Therefore, we used the spin-wave stiffness determined from inelastic neutron scattering [14] for magnon dispersion in our sample. The magnon dispersion for Fe_3GeTe_2 in low energy range can be expressed as $E = E_g + D_1 q_1^2 + D_2 q_2^2 + D_3 q_3^2$, where D_i is the spin-wave stiffness for different directions. Therefore, in the low-energy range, the magnon density of states (DOS) is $N(E) = \Re\frac{\sqrt{E-E_g}}{4\pi^2\sqrt{D_1 D_2 D_3}}$ with D_i constant. The DOS of the magnon increases at a square root rate with energy while keeping at 0 when E $\leq E_g$.

Model calculations

ISTS for quasiparticle excitations

In the following, we introduce the Hamiltonian for scanning tunneling microscopy, which consists of contributions from the tip, the sample, and their hybridization as below:

$$H = H_{tip} + H_{sample} + H_{tunnel}, \tag{1}$$

where H_{tip} is the tip Hamiltonian, H_{sample} is the sample Hamiltonian, and:

$$H_{tunnel} = \sum_{p,k,\sigma} W_{pk} c^{\dagger}_{p\sigma} c_{k\sigma} + H.c. \tag{2}$$

is the hybridization between tip and sample.

The STM tunneling current is

$$\begin{aligned} I = \frac{8\pi e}{\hbar} \int d\varepsilon \sum_{p,k} |W^{\sigma\sigma}_{pk}|^2 [f(\varepsilon) - f(\varepsilon - eU)] \\ \times N_p(\varepsilon) \Im \operatorname{Tr}(G^{\sigma\sigma}(k,\varepsilon)). \end{aligned} \tag{3}$$

where W_{pk} is the tunneling matrix element, and $\Im \operatorname{Tr}(G^{\sigma\sigma}(k,E))$ is the imaginary part of the trace of the spin-resolved retarded Green function of the sample [35, 82, 107, 108]. In general, the tip DOS and tunneling matrix elements do not change much in the low-energy range, and are usually treated as constants.

The measured d^2I/dU^2 signal is

$$\frac{d^2 I}{dU^2}(U) = -\frac{8\pi e}{\hbar} \sum_{p,k} |W_{pk}|^2 N_p(\varepsilon) [\frac{\partial}{\partial \varepsilon} \Im \operatorname{Tr}(G^{\sigma\sigma}(k,\varepsilon))]_{\varepsilon=eU}. \tag{4}$$

The signal is proportional to the imaginary part of the Greens function. The retarded Greens function $G(k,E)$ of the sample can be calculated using the Dyson equation. Expanding the Dyson equation in powers of the self-energy to the lowest order, i.e. $G(k,\varepsilon) = G^0(k,\varepsilon) + G^0(k,\varepsilon)\Sigma(k,\varepsilon)G^0(k,\varepsilon)$, where $G^0(k,\varepsilon)$ is the Green function of the bare electron, typically viewed as responsible for the elastic tunneling current. Note that the DOS $N(\varepsilon) = -\frac{1}{\pi}\Im G^0(\varepsilon)$. The simplified d^2I/dU^2 [35, 109, 110] is below

$$\frac{d^2 I}{dU^2}(U) \approx \sum_{p,k} |W_{pk}|^2 N_p(\varepsilon) N_k(\varepsilon_F)^2 [-\frac{\partial}{\partial \varepsilon} \Im \Sigma(k,\varepsilon)]_{\varepsilon=eU}. \tag{5}$$

The above equation indicates that ISTS is proportional to the derivative of electron self-energy. In comparison with ISTS, we can calculate the derivative of the self-energy due to electron-boson interaction.

For electron-phonon interaction, the spin-resolved electron self-energy according to Migdal theorem [94, 111–114] is

$$\Sigma^{\sigma}_{ep}(\varepsilon) = \sum_{k,q} \int \frac{d\omega}{2\pi} |g_{k,q}|^2 G^{\sigma}(k-q, \varepsilon - \omega) D(q,\omega), \tag{6}$$

with $g_{k,q}$ is the element of the coupling matrix for the electron-phonon coupling. $D(q,\omega)$ is the phonon Green function, with the bare phonon Green function $D_0(q,\omega) = \frac{1}{\omega - \omega_p(q) + i\eta} - \frac{1}{\omega + \omega_p(q) + i\eta}$, ω_p the phonon dispersion, and η positive infinitesimal. When $\omega = \omega_p$, it is the phonon emission, while $\omega = -\omega_p$ corresponds to the phonon absorption.

For electron-magnon interaction in an itinerant ferromagnet, the spin-resolved electron self-energy in random phase approximation [69–71, 115, 116] is

$$\Sigma_{em}^{\sigma}(\varepsilon) = \sum_{k,q} \int \frac{d\omega}{2\pi} |m_{k,q}|^2 G^{\bar{\sigma}}(k-q, \varepsilon - \omega) \chi^{\sigma,\bar{\sigma}}(q,\omega), \tag{7}$$

with $m_{k,q}$ the element of the coupling matrix for electron-magnon coupling. $\chi^{\sigma\bar{\sigma}}(q,\omega) = \frac{\chi_0^{\sigma\bar{\sigma}}(q,\omega)}{1-I_{eff}\chi_0^{\sigma\bar{\sigma}}(q,\omega)}$ is the spin susceptibility, with $\chi_0^{\sigma\bar{\sigma}}(q,\omega) = \sum_k \frac{f(\varepsilon_{k\sigma})-f(\varepsilon_{(k+q)\bar{\sigma}})}{\omega+\varepsilon_{k\sigma}-\varepsilon_{(k+q)\bar{\sigma}}+i\eta}$ the Lindhard function [117] and I_{eff} the effective Stoner parameter. In the energy near the magnon dispersion $\omega_m(q)$, $\chi^{\sigma\bar{\sigma}}(q,\omega) \approx \frac{\chi_0^{\sigma\bar{\sigma}}(q,\omega)}{I_{eff}(\partial \Re \chi_0^{\sigma\bar{\sigma}}(q,\omega)/\partial\omega|_{\omega_m}(\omega-\omega_m(q))+i\Im(\chi_0^{\sigma\bar{\sigma}}(q,\omega)))} - \frac{\chi_0^{\sigma\bar{\sigma}}(q,\omega)}{I_{eff}(\partial \Re \chi_0^{\sigma\bar{\sigma}}(q,\omega)/\partial\omega|_{\omega_m}(\omega+\omega_m(q))+i\Im(\chi_0^{\sigma\bar{\sigma}}(q,\omega)))}$. To make physics clear, we can define the renormalized Green function of the magnon $D(q,\omega) = \frac{Z^{\sigma,\bar{\sigma}}(q,\omega)}{\omega-\omega_m(q)+i\Gamma(q,\omega)} - \frac{Z^{\sigma,\bar{\sigma}}(q,\omega)}{\omega+\omega_m(q)+i\Gamma(q,\omega)}$, where $Z^{\sigma,\bar{\sigma}}(q,\omega) = \frac{\chi_0^{\sigma\bar{\sigma}}(q,\omega)}{I_{eff}\partial \Re \chi_0^{\sigma\bar{\sigma}}(q,\omega)/\partial\omega|_{\omega_m}}$ is the renormalization factor and $\Gamma(q,\omega) = \Im\chi_0^{\sigma\bar{\sigma}}(q,\omega)/(\partial \Re \chi_0^{\sigma\bar{\sigma}}(q,\omega)/\partial\omega|_{\omega_m})$ is the inverse lifetime of the magnon.

The Green functions of a phonon and a magnon in an itinerant ferromagnet are very different. Phonon creation or annihilation depend on the electron-phonon coupling strength. However, in addition to the electron-magnon coupling strength, magnon creation or annihilation are also weighted by the renormalization factor $Z^{\sigma,\bar{\sigma}}(q,\omega)$ determined by the spin-flip scattering between the spin-up and spin-down electronic structure. Generally, $Z^{\sigma,\bar{\sigma}}(0,\omega) \approx 0$, which means that excitation of magnons with very small q is forbidden. In the Stoner continuum, $\Gamma(q,\omega)$ is large, indicating the fast damping of the magnon. Only in the Stoner gap, $\Gamma(q,\omega)$ is very small and a long lifetime magnon exists. Moreover, $Z^{\sigma,\bar{\sigma}}(q,\omega) \neq Z^{\sigma,\bar{\sigma}}(q,-\omega)$. This inequality, together with spin-polarized electron DOS (i.e. $N^{\uparrow}(\varepsilon) \neq N^{\downarrow}(\varepsilon)$), breaks the symmetry of magnon creation and annihilation compared to that of phonon.

Effective Hamiltonian

To calculate the electron self-energy, we derived an effective electron-magnon-polaron interaction model. First of all, we start with the Hamiltonian for an itinerant ferromagnet with strong magnon-phonon coupling. This approximation is reasonable for FGT. Since it has a moderate electron-phonon coupling constant [89, 118], and a comparable electron-magnon coupling constant [89], while the magnetoelastic coupling is strong [18]. With this approximation, we can first diagonalize the Hamiltonian for the magnon and phonon with only magnon-phonon coupling [119–123]. Then, the electron interaction with the magnon polarons was taken into account, and the electron-magnon-polaron coupling matrix elements are obtained. In the end, we obtain an effective Hamiltonian with electron-magnon-polaron interaction.

The Hamiltonian of FGT has electrons, phonons, magnons, and interactions with each other.

$$\begin{aligned} H_{sample} = & \sum_{\sigma,k} \epsilon_{k\sigma} c_{k\sigma}^{\dagger} c_{k\sigma} + \sum_q \hbar\omega_p a_q^{\dagger} a_q + \sum_q \hbar\omega_m b_q^{\dagger} b_q \\ & + \sum_{\sigma,k,q} g_{k,q} c_{(k+q)\sigma}^{\dagger} c_{k\sigma} (a_q + a_{-q}^{\dagger}) \\ & + \sum_{k,q} m_{k,q} (c_{(k+q)\uparrow}^{\dagger} c_{k\downarrow} b_q + c_{(k+q)\downarrow}^{\dagger} c_{k\uparrow} b_{-q}^{\dagger}) \\ & + \sum_q \lambda_q (a_q + a_{-q}^{\dagger})(b_q + b_{-q}^{\dagger}). \end{aligned} \tag{8}$$

with $g_{k,q}$ the electron-phonon coupling matrix element, $m_{k,q}$ the electron-magnon coupling matrix element, and λ_q the magnon-phonon coupling strength. Note that the magnon-phonon coupling term can be diagonalized by Bogoliubov transformation [119, 120]. In fact, $(a_q b^\dagger_{-q} + a^\dagger_{-q} b_q)$ conserves the total number of bosons, while $(a^\dagger_{-q} b^\dagger_{-q} + a_q b_q)$ does not, which is usually ignored [121–123].

The electron-phonon coupling matrix element $g_{k,q}$ is usually small, the electron-magnon coupling matrix element $m_{k,q}$ is large and of the order of the exchange interaction between the local spin S and the electron σ ($J_{\rm ex}\vec{\sigma}\vec{S}$) [69], but is forbidden for low-energy and momentum transfer due to the Stoner gap, that is, there are no pairs of states with small energy difference in bands of opposite spin. The hybridized magnon-phonon mixes spin degrees of freedom with lattice vibrations such that the spin in the lattice becomes ill defined. We will have terms containing magnon-phonon mixing in the Hamiltonian mainly at the crossings of magnons and phonons.

Firstly, without electron-magnon and electron-phonon interactions, the magnon-phonon interactions with total number conservation term only can be diagonalized to magnon polarons following Refs. [121–123], i.e. $A_q = u_q a_q + v_q b_q$, $B_q = u_q b_q - v_q a_q$, where $u_q = \sqrt{\frac{\omega_s+\omega_\delta}{2\omega_s}}$ and $v_q = \sqrt{\frac{\omega_s-\omega_\delta}{2\omega_s}}$ with $\omega_s = \sqrt{\omega_\delta^2 + 4\lambda_q^2}$ and $\omega_\delta = (\omega_m - \omega_p)$ for $\lambda_q \neq 0$ [121, 122]. When $\lambda_q = 0$, $u_q = 1$ and $v_q = 0$. Note that $u_q^2 + v_q^2 = 1$ with u_q and $v_q \in [0, 1]$, indicating the total number conservation of magnon and phonon. At the avoided level crossing, the bosons are equally weighted as $A_q = \frac{a_q+b_q}{\sqrt{2}}$ and $B_q = \frac{b_q-a_q}{\sqrt{2}}$ with $u = v = \sqrt{1/2}$.

Secondly, taking the electron-magnon and electron-phonon interactions into account by using the magnon-polaron basis, we can obtain the Hamiltonian with the electron-magnon-polaron interaction as

$$
\begin{aligned}
H = &\sum_{\sigma,k} \epsilon_{k\sigma} c^\dagger_{k\sigma} c_{k\sigma} + \sum_q \hbar\omega^A_q A^\dagger_q A_q + + \sum_q \hbar\omega^B_q B^\dagger_q B_q + \\
&\sum_{k\sigma,q\sigma'} (\alpha^{\sigma'\sigma}_{k,q}(A_q + A^\dagger_{-q}) + \beta^{\sigma'\sigma}_{k,q}(B_q + B^\dagger_{-q})) c^\dagger_{(k+q)\sigma'} c_{k\sigma},
\end{aligned}
\tag{9}
$$

where electron-magnon-polaron coupling matrix in spin space is below

$$
\begin{aligned}
\alpha_{k,q} &= \begin{pmatrix} g_{k,q}u_q & m_{k,q}v_q \\ m_{k,q}v_q & g_{k,q}u_q \end{pmatrix}, \\
\beta_{k,q} &= \begin{pmatrix} -g_{kq}v_q & m_{k,q}u_q \\ m_{k,q}u_q & -g_{k,q}v_q \end{pmatrix}.
\end{aligned}
\tag{10}
$$

The above Hamiltonian describes the electron-magnon-polaron interactions. It is similar to electron-phonon or electron-magnon interactions. Note, however, that the matrix elements are now mixed, i.e. inelastic excitations are possible with and without spin flip. The strict selection rules that forbid magnon excitation in the Stoner gap are lifted. Therefore, ISTS can be used to efficiently detect magnon polarons.

Based on the above effective Hamiltonian, we can derive the electron self-energy as

$$
\Sigma(\varepsilon) = \sum^{\nu}_{k\sigma,q\sigma'} \int \frac{d\omega}{2\pi} |\gamma^{\sigma\sigma'}_{\nu,k,q}|^2 G^{\sigma'}(k-q, \varepsilon-\omega) D(q,\omega). \tag{11}
$$

Here $\nu = A, B$ is magnon-polaron band index, and $D(q,\omega)$ is now the Green function of magnon-polaron. When $\sigma' = \sigma$, $D(q,\omega) = \frac{1}{\omega-\omega_{mp}(q)+i\Gamma_{ep}} - \frac{1}{\omega+\omega_{mp}(q)+i\Gamma_{ep}}$, where $\omega_{mp}(q)$ is the magnon polaron dispersion and Γ_{ep} the inverse lifetime due to the electron-phonon interaction. However, when $\sigma' = \bar{\sigma}$, $D(q,\omega) = \frac{Z(q,\omega)}{\omega-\omega_{mp}(q)+i\Gamma_{em}} - \frac{Z(q,\omega)}{\omega+\omega_{mp}(q)+i\Gamma_{em}}$ with Γ_{em} the inverse lifetime due to the electron-magnon interaction.

ISTS for magnon polaron excitations

Here we start from the effective Hamiltonian obtained to calculate the derivative of imaginary part of electron self-energy as a result of electron-magnon polaron interactions, which incorporate electrons, phonons, magnons and interactions between each other. As an implementation with ab initio dispersions of all these three quasiparticles is currently not feasible due to computational limits, we focus on the physics of this problem using empirical models for these quasiparticles, i.e. free electron model with exchange splitting, Debye model for acoustic phonon, and quadratic dispersion for magnon. To highlight the magnon-phonon coupling induced selection, we use minimal assumptions for the interactions between electron, phonon and magnon, i.e. treating the electron-phonon coupling matrix element $g_{k,q}$ (≈ 0.01 eV for a moderate electron-phonon interaction [89]), the electron-magnon coupling matrix element $m_{k,q}$ ($\approx \frac{\Delta_{ex}}{S} = 1.4$ eV with $\Delta_{ex} = 1.05$ eV and $S = 0.74$ for FGT [18]), and the magnon-phonon coupling matrix element λ_q as constants. Note that no magnon-phonon coupling strength is reported for FGT, but for $FePS_3$ the reported hybridization gap is ≈ 0.25 meV [66]. In the Stoner gap, $Z^{\sigma,\bar{\sigma}}(q,\omega)(\approx 0.001) << 1$ and $\Gamma(q,\omega)$ is very small. Then, only the electron-magnon-polaron coupling matrix is q-dependent, i.e. α_q and β_q. Moreover, this momentum dependence originates from the q-dependent u_q and v_q, which depends on the magnon-phonon coupling. With these approximations, we obtained the derivative of imaginary part of self-energy as below

$$-\partial\Im\Sigma(\varepsilon)/\partial\varepsilon \approx \mathrm{sgn}(\varepsilon)\sum_{\nu,\sigma}[|\gamma_\nu^{\sigma,\sigma}|^2 N^\sigma(E_F) + |\gamma_\nu^{\sigma,\bar{\sigma}}|^2 |Z^{\sigma,\bar{\sigma}}| N^{\bar{\sigma}}(E_F)]F_\nu(\varepsilon). \tag{12}$$

Here $F_\nu(\varepsilon)$ is the magnon-polaron DOS with band index, and $N^\sigma(E_F)$ is the spin-resolved electron DOS at Fermi energy. According to Eq. (2), $d^2I/dU^2 \propto$ Eq. (12). We note that the damping of the phonon and magnon due to electrons is not considered, resulting in an energy-dependent decay behavior as observed in experiments.

Data availability

All relevant data are available from the corresponding authors on request. Source data are provided in this paper and supplementary information.

References

[1] Je-Geun Park. Opportunities and challenges of 2d magnetic van der waals materials: magnetic graphene? *J. Phys. Condens. Matter*, 28(30):301001, june 2016.

[2] Bevin Huang, Genevieve Clark, Efrén Navarro-Moratalla, Dahlia R. Klein, Ran Cheng, Kyle L. Seyler, Ding Zhong, Emma Schmidgall, Michael A. McGuire, David H. Cobden,

Wang Yao, Di Xiao, Pablo Jarillo-Herrero, and Xiaodong Xu. Layer-dependent ferromagnetism in a van der waals crystal down to the monolayer limit. *Nature*, 546(7657):270–273, 2017.

[3] C. Gong, L. Li, Z. Li, H. Ji, A. Stern, Y. Xia, T. Cao, W. Bao, C. Wang, Y. Wang, Z. Q. Qiu, R. J. Cava, S. G. Louie, J. Xia, and X. Zhang. Discovery of intrinsic ferromagnetism in two-dimensional van der waals crystals. *Nature*, 546(7657):265–269, 2017.

[4] Kenneth S. Burch, David Mandrus, and Je-Geun Park. Magnetism in two-dimensional van der waals materials. *Nature*, 563(7729):47–52, 2018.

[5] Babar Shabbir, Muhammad Nadeem, Zhigao Dai, Michael S Fuhrer, Qi-Kun Xue, Xiaolin Wang, and Qiaoliang Bao. Long range intrinsic ferromagnetism in two dimensional materials and dissipationless future technologies. *Appl. Phys. Rev.*, 5(4):041105, 2018.

[6] M. Gibertini, M. Koperski, A. F. Morpurgo, and K. S. Novoselov. Magnetic 2d materials and heterostructures. *Nat. Nanotechnol.*, 14(5):408–419, 2019.

[7] Cheng Gong and Xiang Zhang. Two-dimensional magnetic crystals and emergent heterostructure devices. *Science*, 363(6428):eaav4450, 2019.

[8] Hui Li, Shuangchen Ruan, and Yu-Jia Zeng. Intrinsic van der waals magnetic materials from bulk to the 2d limit: New frontiers of spintronics. *Adv. Mater.*, 31(27):1900065, 2019.

[9] Meng-Chien Wang, Che-Chun Huang, Chi-Ho Cheung, Chih-Yu Chen, Seng Ghee Tan, Tsung-Wei Huang, Yue Zhao, Yanfeng Zhao, Gang Wu, Yuan-Ping Feng, Han-Chun Wu, and Ching-Ray Chang. Prospects and opportunities of 2d van der waals magnetic systems. *Ann. Phys.*, 532(5):1900452, 2020.

[10] Qing Hua Wang, Amilcar Bedoya-Pinto, Mark Blei, Avalon H. Dismukes, Assaf Hamo, Sarah Jenkins, Maciej Koperski, Yu Liu, Qi-Chao Sun, Evan J. Telford, Hyun Ho Kim, Mathias Augustin, Uri Vool, Jia-Xin Yin, Lu Hua Li, Alexey Falin, Cory R. Dean, Fèlix Casanova, Richard F. L. Evans, Mairbek Chshiev, Artem Mishchenko, Cedomir Petrovic, Rui He, Liuyan Zhao, Adam W. Tsen, Brian D. Gerardot, Mauro Brotons-Gisbert, Zurab Guguchia, Xavier Roy, Sefaattin Tongay, Ziwei Wang, M. Zahid Hasan, Joerg Wrachtrup, Amir Yacoby, Albert Fert, Stuart Parkin, Kostya S. Novoselov, Pengcheng Dai, Luis Balicas, and Elton J. G. Santos. The magnetic genome of two-dimensional van der waals materials. *ACS Nano*, 16(5):6960–7079, 2022.

[11] EJ Samuelsen, Richard Silberglitt, G Shirane, and JP Remeika. Spin waves in ferromagnetic cr br 3 studied by inelastic neutron scattering. *Phys. Rev. B*, 3(1):157, 1971.

[12] A. R. Wildes, B. Roessli, B. Lebech, and K. W. Godfrey. Spin waves and the critical behaviour of the magnetization in. *J. Phys. Condens. Matter.*, 10(28):6417, 1998.

[13] S Calder, Alexander I Kolesnikov, and Andrew F May. Magnetic excitations in the quasi-two-dimensional ferromagnet fe 3- x gete 2 measured with inelastic neutron scattering. *Phys. Rev. B*, 99(9):094423, 2019.

[14] Song Bao, Wei Wang, Yanyan Shangguan, Zhengwei Cai, Zhao-Yang Dong, Zhentao Huang, Wenda Si, Zhen Ma, Ryoichi Kajimoto, Kazuhiko Ikeuchi, et al. Neutron spectroscopy evidence on the dual nature of magnetic excitations in a van der waals metallic ferromagnet fe 2.72 gete 2. *Phys. Rev. X*, 12(1):011022, 2022.

[15] Xiaojian Bai, Frank Lechermann, Yaohua Liu, Yongqiang Cheng, Alexander I. Kolesnikov, Feng Ye, Travis J. Williams, Songxue Chi, Tao Hong, Garrett E. Granroth, Andrew F. May, and Stuart Calder. Antiferromagnetic fluctuations and orbital-selective mott transition in the van der waals ferromagnet $fe_{3-x}gete_2$. *Phys. Rev. B*, 106(18):L180409, 2022.

[16] Marcio Costa, Nuno MR Peres, Joaquín Fernández-Rossier, and António T Costa. Nonreciprocal magnons in a two-dimensional crystal with out-of-plane magnetization. *Phys. Rev. B*, 102(1):014450, 2020.

[17] Tingting Yin, Kanchan Ajit Ulman, Sheng Liu, Andrés Granados del Águila, Yuqing Huang, Lifa Zhang, Marco Serra, David Sedmidubsky, Zdenek Sofer, Su Ying Quek, and Qihua Xiong. Chiral phonons and giant magneto-optical effect in crbr3 2d magnet. *Adv. Mater.*, 33(36):2101618, 2021.

[18] Houlong L Zhuang, PRC Kent, and Richard G Hennig. Strong anisotropy and magnetostriction in the two-dimensional stoner ferromagnet fe 3 gete 2. *Phys. Rev. B*, 93(13):134407, 2016.

[19] Lucas Webster and Jia-An Yan. Strain-tunable magnetic anisotropy in monolayer $crcl_3$, $crbr_3$, and cri_3. *Phys. Rev. B*, 98(14):144411, 2018.

[20] Imran Khan and Jisang Hong. High curie temperature and strain-induced semiconductor-metal transition with spin reorientation transition in 2d crpbte3 monolayer. *Nanotechnology*, 31(19):195704, 2020.

[21] Yu Wang, Cong Wang, Shi-Jun Liang, Zecheng Ma, Kang Xu, Xiaowei Liu, Lili Zhang, Alemayehu S. Admasu, Sang-Wook Cheong, Lizheng Wang, Moyu Chen, Zenglin Liu, Bin Cheng, Wei Ji, and Feng Miao. Strain-sensitive magnetization reversal of a van der waals magnet. *Adv. Mater.*, 32(42):2004533, 2020.

[22] Xiaohui Hu, Yinghe Zhao, Xiaodong Shen, Arkady V. Krasheninnikov, Zhongfang Chen, and Litao Sun. Enhanced ferromagnetism and tunable magnetism in fe3gete2 monolayer by strain engineering. *ACS Appl. Mater. Interfaces*, 12(23):26367–26373, 2020.

[23] Dorye L. Esteras, Andrey Rybakov, Alberto M. Ruiz, and José J. Baldoví. Magnon straintronics in the 2d van der waals ferromagnet crsbr from first-principles. *Nano Lett.*, 22(21):8771–8778, 2022.

[24] T Balashov, AF Takács, W Wulfhekel, and J Kirschner. Magnon excitation with spin-polarized scanning tunneling microscopy. *Phys. Rev. Lett.*, 97(18):187201, 2006.

[25] T Balashov, AF Takács, M Däne, A Ernst, P Bruno, and W Wulfhekel. Inelastic electron-magnon interaction and spin transfer torque. *Phys. Rev. B*, 78(17):174404, 2008.

[26] C. L. Gao, A. Ernst, G. Fischer, W. Hergert, P. Bruno, W. Wulfhekel, and J. Kirschner. Spin wave dispersion on the nanometer scale. *Phys. Rev. Lett.*, 101(16):167201, 2008.

[27] T. Balashov, P. Buczek, L. Sandratskii, A. Ernst, and W. Wulfhekel. Magnon dispersion in thin magnetic films. *J. Phys. Condens. Matter*, 26(39):394007, 2014.

[28] Anna Spinelli, Benjamin Bryant, Fernando Delgado, Joaquín Fernández-Rossier, and Alexander F Otte. Imaging of spin waves in atomically designed nanomagnets. *Nat. Mater.*, 13(8):782–785, 2014.

[29] Michael Schackert, Tobias Märkl, Jasmin Jandke, Martin Hölzer, Sergey Ostanin, Eberhard KU Gross, Arthur Ernst, and Wulf Wulfhekel. Local measurement of the eliashberg function of pb islands: Enhancement of electron-phonon coupling by quantum well states. *Phys. Rev. Lett.*, 114(4):047002, 2015.

[30] Jasmin Jandke, Patrik Hlobil, Michael Schackert, Wulf Wulfhekel, and Jörg Schmalian. Coupling to real and virtual phonons in tunneling spectroscopy of superconductors. *Phys. Rev. B*, 93(6):060505, 2016.

[31] Jasmin Jandke, Fang Yang, Patrik Hlobil, Tobias Engelhardt, Dominik Rau, Khalil Zakeri, Chunlei Gao, Jörg Schmalian, and Wulf Wulfhekel. Unconventional pairing in single fese layers. *Phys. Rev. B*, 100:020503, Jul 2019.

[32] Barry C Stipe, Mohammad A Rezaei, and Wilson Ho. Single-molecule vibrational spectroscopy and microscopy. *Science*, 280(5370):1732–1735, 1998.

[33] H. Gawronski, M. Mehlhorn, and K. Morgenstern. Imaging phonon excitation with atomic resolution. *Science*, 319(5865):930–933, 2008.

[34] K. Volgmann, H. Gawronski, Ch Zaum, G. G. Rusina, S. D. Borisova, E. V. Chulkov, and K. Morgenstern. Local determination of the amount of integration of an atom into a crystal surface. *Nat. Commun.*, 5(1):5089, 2014.

[35] Emi Minamitani, Ryuichi Arafune, Noriyuki Tsukahara, Yoshitaka Ohda, Satoshi Watanabe, Maki Kawai, Hiromu Ueba, and Noriaki Takagi. Surface phonon excitation on clean metal surfaces in scanning tunneling microscopy. *Phys. Rev. B*, 93(8):085411, 2016.

[36] Yuanbo Zhang, Victor W. Brar, Feng Wang, Caglar Girit, Yossi Yayon, Melissa Panlasigui, Alex Zettl, and Michael F. Crommie. Giant phonon-induced conductance in scanning tunneling spectroscopy of gate-tunable graphene. *Nat. Phys.*, 4(8):627–630, 2008.

[37] Hyo Won Kim, Wonhee Ko, JiYeon Ku, Insu Jeon, Donggyu Kim, Hyeokshin Kwon, Youngtek Oh, Seunghwa Ryu, Young Kuk, Sung Woo Hwang, and Hwansoo Suh. Nanoscale control of phonon excitations in graphene. *Nat. Commun.*, 6(1):7528, 2015.

[38] Hans-Jörg Deiseroth, Krasimir Aleksandrov, Christof Reiner, Lorenz Kienle, and Reinhard K. Kremer. Fe3gete2 and ni3gete2 – two new layered transition-metal compounds: Crystal structures, hrtem investigations, and magnetic and electrical properties. *Eur. J. Inorg. Chem.*, 2006(8):1561–1567, 2006.

[39] Bin Chen, JinHu Yang, HangDong Wang, Masaki Imai, Hiroto Ohta, Chishiro Michioka, Kazuyoshi Yoshimura, and MingHu Fang. Magnetic properties of layered itinerant electron ferromagnet fe3gete2. *J. Phys. Soc. Japan*, 82(12):124711, 2013.

[40] Cheng Tan, Jinhwan Lee, Soon-Gil Jung, Tuson Park, Sultan Albarakati, James Partridge, Matthew R Field, Dougal G McCulloch, Lan Wang, and Changgu Lee. Hard magnetic properties in nanoflake van der waals fe3gete2. *Nat. Commun.*, 9(1):1554, 2018.

[41] Yujun Deng, Yijun Yu, Yichen Song, Jingzhao Zhang, Nai Zhou Wang, Zeyuan Sun, Yangfan Yi, Yi Zheng Wu, Shiwei Wu, Junyi Zhu, et al. Gate-tunable room-temperature ferromagnetism in two-dimensional fe3gete2. *Nature*, 563(7729):94–99, 2018.

[42] Yun Zhang, Haiyan Lu, Xiegang Zhu, Shiyong Tan, Wei Feng, Qin Liu, Wen Zhang, Qiuyun Chen, Yi Liu, Xuebing Luo, et al. Emergence of kondo lattice behavior in a van der waals itinerant ferromagnet, fe3gete2. *Sci. Adv.*, 4(1):eaao6791, 2018.

[43] Giang D Nguyen, Jinhwan Lee, Tom Berlijn, Qiang Zou, Saban M Hus, Jewook Park, Zheng Gai, Changgu Lee, and An-Ping Li. Visualization and manipulation of magnetic domains in the quasi-two-dimensional material f e 3 get e 2. *Phys. Rev. B*, 97(1):014425, 2018.

[44] Xiangru Kong, Giang D. Nguyen, Jinhwan Lee, Changgu Lee, Stuart Calder, Andrew F. May, Zheng Gai, An-Ping Li, Liangbo Liang, and Tom Berlijn. Interlayer magnetism in $fe_{3-x}gete_2$. *Phys. Rev. Mater.*, 4(9):094403, 2020.

[45] Hung-Hsiang Yang, Namrata Bansal, Philipp Rüßmann, Markus Hoffmann, Lichuan Zhang, Dongwook Go, Qili Li, Amir-Abbas Haghighirad, Kaushik Sen, Stefan Blügel, et al. Magnetic domain walls of the van der waals material fe3gete2. *2D Mater.*, 9(2):025022, 2022.

[46] Christopher Trainer, Olivia R Armitage, Harry Lane, Luke C Rhodes, Edmond Chan, Izidor Benedičič, Jose A Rodriguez-Rivera, Oscar Fabelo, Chris Stock, and Peter Wahl. Relating spin-polarized stm imaging and inelastic neutron scattering in the van der waals ferromagnet fe 3 gete 2. *Phys. Rev. B*, 106(8):L081405, 2022.

[47] Bei Ding, Zefang Li, Guizhou Xu, Hang Li, Zhipeng Hou, Enke Liu, Xuekui Xi, Feng Xu, Yuan Yao, and Wenhong Wang. Observation of magnetic skyrmion bubbles in a van der waals ferromagnet fe3gete2. *Nano Lett.*, 20(2):868–873, 2020.

[48] Tae-Eon Park, Licong Peng, Jinghua Liang, Ali Hallal, Fehmi Sami Yasin, Xichao Zhang, Kyung Mee Song, Sung Jong Kim, Kwangsu Kim, Markus Weigand, Gisela Schütz, Simone Finizio, Jörg Raabe, Karin Garcia, Jing Xia, Yan Zhou, Motohiko Ezawa, Xiaoxi Liu, Joonyeon Chang, Hyun Cheol Koo, Young Duck Kim, Mairbek Chshiev, Albert Fert, Hongxin Yang, Xiuzhen Yu, and Seonghoon Woo. Neel-type skyrmions and their current-induced motion in van der waals ferromagnet-based heterostructures. *Phys. Rev. B*, 103(10):104410, 2021.

[49] M. T. Birch, L. Powalla, S. Wintz, O. Hovorka, K. Litzius, J. C. Loudon, L. A. Turnbull, V. Nehruji, K. Son, C. Bubeck, T. G. Rauch, M. Weigand, E. Goering, M. Burghard, and G. Schütz. History-dependent domain and skyrmion formation in 2d van der waals magnet fe3gete2. *Nat. Commun.*, 13(1):3035, 2022.

[50] Yue Li, Rabindra Basnet, Krishna Pandey, Jin Hu, Wei Wang, Xuedan Ma, Arthur RC McCray, Amanda K Petford-Long, and Charudatta Phatak. Field-dependent magnetic domain behavior in van der waals fe3gete2. *JOM*, 74(6):2310–2318, 2022.

[51] Mariëlle J. Meijer, Juriaan Lucassen, Rembert A. Duine, Henk J. M. Swagten, Bert Koopmans, Reinoud Lavrijsen, and Marcos H. D. Guimarães. Chiral spin spirals at the surface of the van der waals ferromagnet fe3gete2. *Nano Lett.*, 20(12):8563–8568, 2020.

[52] Zaiyao Fei, Bevin Huang, Paul Malinowski, Wenbo Wang, Tiancheng Song, Joshua Sanchez, Wang Yao, Di Xiao, Xiaoyang Zhu, Andrew F May, et al. Two-dimensional itinerant ferromagnetism in atomically thin fe3gete2. *Nat. Mater.*, 17(9):778–782, 2018.

[53] Neliza León-Brito, Eric Dietzgen Bauer, Filip Ronning, Joe David Thompson, and Roman Movshovich. Magnetic microstructure and magnetic properties of uniaxial itinerant ferromagnet fe3gete2. *J. Appl. Phys.*, 120(8):083903, 2016.

[54] Yun-Peng Wang, Xiao-Yan Chen, and Meng-Qiu Long. Modifications of magnetic anisotropy of fe3gete2 by the electric field effect. *Appl. Phys. Lett.*, 116(9):092404, 2020.

[55] Dongzhe Li, Soumyajyoti Haldar, Tim Drevelow, and Stefan Heinze. Tuning the magnetic interactions in van der waals fe_3gete_2 heterostructures: A comparative study of ab initio methods. *Phys. Rev. B*, 107:104428, Mar 2023.

[56] Yurong You, Yuanyuan Gong, Hang Li, Zefang Li, Mengmei Zhu, Jiaxuan Tang, Enke Liu, Yuan Yao, Guizhou Xu, Feng Xu, and Wenhong Wang. Angular dependence of the topological hall effect in the uniaxial van der waals ferromagnet fe_3gete_2. *Phys. Rev. B*, 100:134441, Oct 2019.

[57] Andrew F May, Stuart Calder, Claudia Cantoni, Huibo Cao, and Michael A McGuire. Magnetic structure and phase stability of the van der waals bonded ferromagnet fe 3- x gete 2. *Phys. Rev. B*, 93(1):014411, 2016.

[58] Valeriy Yu Verchenko, Alexander A Tsirlin, Alexei V Sobolev, Igor A Presniakov, and Andrei V Shevelkov. Ferromagnetic order, strong magnetocrystalline anisotropy, and magnetocaloric effect in the layered telluride fe3- δgete2. *Inorg. Chem.*, 54(17):8598–8607, 2015.

[59] Luojun Du, Jian Tang, Yanchong Zhao, Xiaomei Li, Rong Yang, Xuerong Hu, Xueyin Bai, Xiao Wang, Kenji Watanabe, Takashi Taniguchi, Dongxia Shi, Guoqiang Yu, Xuedong Bai, Tawfique Hasan, Guangyu Zhang, and Zhipei Sun. Lattice dynamics, phonon chirality, and spin–phonon coupling in 2d itinerant ferromagnet fe3gete2. *Adv. Funct. Mater.*, 29(48):1904734, 2019.

[60] Xiangru Kong, Tom Berlijn, and Liangbo Liang. Thickness and spin dependence of raman modes in magnetic layered fe3gete2. *Adv. Electron. Mater.*, 7(7):2001159, 2021.

[61] Qingan Cai, Yuemei Zhang, Diana Luong, Christopher A. Tulk, Boniface P. T. Fokwa, and Chen Li. Spin–phonon interactions and anharmonic lattice dynamics in fe3gete2. *Adv. Phys. Res.*, page 2200089, 2023.

[62] Haoran Man, Zhong Shi, Guangyong Xu, Yadong Xu, Xi Chen, Sean Sullivan, Jianshi Zhou, Ke Xia, Jing Shi, and Pengcheng Dai. Direct observation of magnon-phonon coupling in yttrium iron garnet. *Phys. Rev. B*, 96(10):100406, 2017.

[63] Junxue Li, Haakon T. Simensen, Derek Reitz, Qiyang Sun, Wei Yuan, Chen Li, Yaroslav Tserkovnyak, Arne Brataas, and Jing Shi. Observation of magnon polarons in a uniaxial antiferromagnetic insulator. *Phys. Rev. Lett.*, 125(21):217201, 2020.

[64] Sheng Liu, Andrés Granados del Águila, Dhiman Bhowmick, Chee Kwan Gan, T. Thu Ha Do, M. A. Prosnikov, David Sedmidubský, Zdenek Sofer, Peter C. M. Christianen, Pinaki Sengupta, and Qihua Xiong. Direct observation of magnon-phonon strong coupling in two-dimensional antiferromagnet at high magnetic fields. *Phys. Rev. Lett.*, 127(9):097401, 2021.

[65] D. Vaclavkova, M. Palit, J. Wyzula, S. Ghosh, A. Delhomme, S. Maity, P. Kapuscinski, A. Ghosh, M. Veis, M. Grzeszczyk, C. Faugeras, M. Orlita, S. Datta, and M. Potemski. Magnon polarons in the van der waals antiferromagnet $Feps_3$. *Phys. Rev. B*, 104(13):134437, 2021.

[66] Jun Cui, Emil Viñas Boström, Mykhaylo Ozerov, Fangliang Wu, Qianni Jiang, Jiun-Haw Chu, Changcun Li, Fucai Liu, Xiaodong Xu, Angel Rubio, and Qi Zhang. Chirality selective magnon-phonon hybridization and magnon-induced chiral phonons in a layered zigzag antiferromagnet. *Nat. Commun.*, 14(1):3396, 2023.

[67] Jiaming Luo, Shuyi Li, Zhipeng Ye, Rui Xu, Han Yan, Junjie Zhang, Gaihua Ye, Lebing Chen, Ding Hu, Xiaokun Teng, et al. Evidence for topological magnon–phonon hybridization in a 2d antiferromagnet down to the monolayer limit. *Nano Lett.*, 23(5):2023–2030, 2023.

[68] Edward L Wolf. *Principles of electron tunneling spectroscopy.* Oxford University Press, Oxford, 2011.

[69] L. C. Davis and S. H. Liu. Electron-magnon interaction in ferromagnetic transition metals. *Phys. Rev.*, 163(2):503–505, 1967.

[70] D. M. Edwards and J. A. Hertz. Electron-magnon interactions in itinerant ferromagnetism. ii. strong ferromagnetism. *J. Phys. F: Met. Phys.*, 3(12):2191, 1973.

[71] J. A. Hertz and D. M. Edwards. Electron-magnon interactions in itinerant ferromagnetism. i. formal theory. *J. Phys. F: Met. Phys.*, 3(12):2174, 1973.

[72] Carmen Rubio-Verdu and Katharina J. Franke. Signatures of kondo-lattice behavior in the two-dimensional ferromagnet fe3gete2. *arXiv:2505.02698*, 2025.

[73] O. Ujsaghy, J. Kroha, L. Szunyogh, and A. Zawadowski. Theory of the fano resonance in the stm tunneling density of states due to a single kondo impurity. *Phys. Rev. Lett.*, 85(12):2557–2560, 2000.

[74] Benedikt Schweflinghaus, Manuel dos Santos Dias, Antonio T. Costa, and Samir Lounis. Renormalization of electron self-energies via their interaction with spin excitations: A first-principles investigation. *Phys. Rev. B*, 89(23):235439, 2014.

[75] Juba Bouaziz, Filipe Souza Mendes Guimarães, and Samir Lounis. A new view on the origin of zero-bias anomalies of co atoms atop noble metal surfaces. *Nat. Commun.*, 11(1):6112, 2020.

[76] Felix Friedrich, Artem Odobesko, Juba Bouaziz, Samir Lounis, and Matthias Bode. Evidence for spinarons in co adatoms. *Nat. Phys.*, 20(1), 2024.

[77] B. L. Altshuler, A. G. Aronov, and P. A. Lee. Interaction effects in disordered fermi systems in two dimensions. *Phys. Rev. Lett.*, 44(19):1288–1291, 1980.

[78] J. M. Rowell and L. Y. L. Shen. Zero-bias anomalies in normal metal tunnel junctions. *Phys. Rev. Lett.*, 17(1):15–19, 1966.

[79] Jagadeesh S. Moodera, Janusz Nowak, and Rene J. M. van de Veerdonk. Interface magnetism and spin wave scattering in ferromagnet-insulator-ferromagnet tunnel junctions. *Phys. Rev. Lett.*, 80(13):2941–2944, 1998.

[80] Y. Ando, J. Murai, H. Kubota, and T. Miyazaki. Magnon-assisted inelastic excitation spectra of a ferromagnetic tunnel junction. *J. Appl. Phys.*, 87(9):5209–5211, 2000.

[81] V. Drewello, J. Schmalhorst, A. Thomas, and G. Reiss. Evidence for strong magnon contribution to the tmr temperature dependence in mgo based tunnel junctions. *Phys. Rev. B*, 77(1):014440, 2008.

[82] Jerry Tersoff and Donald R Hamann. Theory of the scanning tunneling microscope. *Phys. Rev. B*, 31(2):805, 1985.

[83] Christian R. Ast, Berthold Jäck, Jacob Senkpiel, Matthias Eltschka, Markus Etzkorn, Joachim Ankerhold, and Klaus Kern. Sensing the quantum limit in scanning tunnelling spectroscopy. *Nat. Commun.*, 7(1):13009, 2016.

[84] J. Senkpiel, J. C. Klockner, M. Etzkorn, S. Dambach, B. Kubala, W. Belzig, A. L. Yeyati, J. C. Cuevas, F. Pauly, J. Ankerhold, C. R. Ast, and K. Kern. Dynamical coulomb blockade as a local probe for quantum transport. *Phys. Rev. Lett.*, 124(15):156803, 2020.

[85] Taner Esat, Markus Ternes, Ruslan Temirov, and F. Stefan Tautz. Electron spin secluded inside a bottom-up assembled standing metal-molecule nanostructure. *Phys. Rev. Res.*, 5:033200, Sep 2023.

[86] Michel Julliere. Tunneling between ferromagnetic films. *Phys. Lett. A*, 54(3):225–226, 1975.

[87] A. Kubetzka, M. Bode, O. Pietzsch, and R. Wiesendanger. Spin-polarized scanning tunneling microscopy with antiferromagnetic probe tips. *Phys. Rev. Lett.*, 88(5):057201, 2002.

[88] S. Zhang, P. M. Levy, A. C. Marley, and S. S. P. Parkin. Quenching of magnetoresistance by hot electrons in magnetic tunnel junctions. *Phys. Rev. Lett.*, 79:3744–3747, Nov 1997.

[89] Danis I. Badrtdinov, Georgy V. Pushkarev, Mikhail I. Katsnelson, and Alexander N. Rudenko. Electron transport and scattering mechanisms in ferromagnetic monolayer fe3gete2. *npj 2D Materials and Applications*, 7(1):52, 2023.

[90] Charles Kittel. Physical theory of ferromagnetic domains. *Rev. Mod. Phys.*, 21:541–583, Oct 1949.

[91] R. D. McMichael and Andrew Kunz. Calculation of damping rates in thin inhomogeneous ferromagnetic films due to coupling to lattice vibrations. *J. Appl. Phys.*, 91(10):8650–8652, 05 2002.

[92] B. N. Brockhouse and A. T. Stewart. Normal modes of aluminum by neutron spectrometry. *Rev. Mod. Phys.*, 30(1):236–249, 1958.

[93] Richard T. Harley, John B. Page, and Charles T. Walker. Raman scattering as a probe of pure-crystal phonons in $\mathrm{t1}^{+}$ -doped potassium halides. *Phys. Rev. Lett.*, 23(16):922–924, 1969.

[94] S. Engelsberg and J. R. Schrieffer. Coupled electron-phonon system. *Phys. Rev.*, 131(3):993–1008, 1963.

[95] M. Lavagna, C. Lacroix, and M. Cyrot. Electrical resistivity of the kondo lattice. *Journal of Applied Physics*, 53(3):2055–2057, 1982.

[96] Timofey Balashov, Michael Meyer, and Wulf Wulfhekel. A compact ultrahigh vacuum scanning tunneling microscope with dilution refrigeration. *Rev. Sci. Instrum.*, 89(11):113707, 2018.

[97] G. G. Kresse and J.J. Furthmüller. Efficient iterative schemes for ab initio total-energy calculations using a plane-wave basis set. *Phys. Rev. B*, 54:11169, 1996.

[98] J. P. Perdew and A. Zunger. Self-interaction correction to density-functional approximations for many-body systems. *Phys. Rev. B*, 23(10):5048–5079, 1981.

[99] G. Kresse and D. Joubert. From ultrasoft pseudopotentials to the projector augmented-wave method. *Phys. Rev. B*, 59(3):1758–1775, 1999.

[100] Hendrik J Monkhorst and James D Pack. Special points for brillouin-zone integrations. *Phys. Rev. B*, 13(12):5188, 1976.

[101] K. Parlinski, Z. Q. Li, and Y. Kawazoe. First-principles determination of the soft mode in cubic zro$_2$. *Phys. Rev. Lett.*, 78(21):4063–4066, 1997.

[102] Atsushi Togo, Fumiyasu Oba, and Isao Tanaka. First-principles calculations of the ferroelastic transition between rutile-type and cacl 2-type sio 2 at high pressures. *Phys. Rev. B*, 78(13):134106, 2008.

[103] Charles Kittel. On the theory of ferromagnetic resonance absorption. *Phys. Rev.*, 73(2):155–161, 1948.

[104] J. M. Beaujour, D. Ravelosona, I. Tudosa, E. E. Fullerton, and A. D. Kent. Ferromagnetic resonance linewidth in ultrathin films with perpendicular magnetic anisotropy. *Phys. Rev. B*, 80(18):180415, 2009.

[105] Khalil Zakeri. Elementary spin excitations in ultrathin itinerant magnets. *Phys. Rep.*, 545(2):47–93, 2014.

[106] Zhixue Shu, Shufeng Zhang, and Tai Kong. Spin stiffness and spin excitation gap of van der waals ferromagnetic $Fe_{3+\delta}GeTe_2$. *J. Phys. Condens. Matter*, 36(38):385801, 2024.

[107] J. Bardeen. Tunnelling from a many-particle point of view. *Phys. Rev. Lett.*, 6(2):57–59, 1961.

[108] Jiutao Li, Wolf-Dieter Schneider, Richard Berndt, O. R. Bryant, and S. Crampin. Surface-state lifetime measured by scanning tunneling spectroscopy. *Phys. Rev. Lett.*, 81(20):4464–4467, 1998.

[109] C. Caroli, R. Combescot, P. Nozieres, and D. Saint-James. A direct calculation of the tunnelling current: Iv. electron-phonon interaction effects. *J. Phys. C: Solid State Phys.*, 5(1):21, 1972.

[110] Emi Minamitani, Noriaki Takagi, Ryuichi Arafune, Thomas Frederiksen, Tadahiro Komeda, Hiromu Ueba, and Satoshi Watanabe. Inelastic electron tunneling spectroscopy by stm of phonons at solid surfaces and interfaces. *Prog. Surf. Sci.*, 93(4):131–145, 2018.

[111] H. Y. Fan. Temperature dependence of the energy gap in semiconductors. *Phys. Rev.*, 82(6):900–905, 1951.

[112] A. B. Migdal. Interaction between electrons and lattice vibrations in a normal metal. *Sov. Phys. JETP.*, 34:996–1001, 1958.

[113] G. M. Eliashberg. Interactions between electrons and lattice viera tions in a superconductor. *Sov. Phys. JETP*, 11:696, 1960.

[114] G. Grimvall. The electron-phonon interaction in normal metals. *Physica Scripta*, 14(1-2):63, 1976.

[115] Mathias C. T. D. Müller, Stefan Blügel, and Christoph Friedrich. Electron-magnon scattering in elementary ferromagnets from first principles: Lifetime broadening and band anomalies. *Phys. Rev. B*, 100(4):045130, 2019.

[116] Dmitrii Nabok, Stefan Blügel, and Christoph Friedrich. Electron–plasmon and electron–magnon scattering in ferromagnets from first principles by combining gw and gt self-energies. *npj Computational Materials*, 7(1):178, 2021.

[117] Jens Lindhard. On the properties of a gas of charged particles. *K. Dan. Vidensk. Selsk. Mat. Fys. Medd.*, 28, 1954.

[118] Danis I. Badrtdinov, Mikhail I. Katsnelson, and Alexander N. Rudenko. Phonon-induced renormalization of exchange interactions in metallic two-dimensional magnets. *Phys. Rev. B*, 110(6):L060409, 2024.

[119] N. Bogoliubov. On the theory of superfluidity. *J. Phys. USSR*, 11:23–32, 1947.

[120] N. N. Bogoliubov, V. V. Tolmachov, and D. V. Širkov. A new method in the theory of superconductivity. *Fortschr. Phys.*, 6(11-12):605–682, 1958.

[121] S. C. Guerreiro and S. M. Rezende. Quantum theory of the magnon-phonon interaction in a time-dependent magnetic field. *Rev. Bras. Fis.*, 1:207, 1971.

[122] Sergio C. Guerreiro and Sergio M. Rezende. Magnon-phonon interconversion in a dynamically reconfigurable magnetic material. *Phys. Rev. B*, 92(21):214437, 2015.

[123] Gyungchoon Go, Se Kwon Kim, and Kyung-Jin Lee. Topological magnon-phonon hybrid excitations in two-dimensional ferromagnets with tunable chern numbers. *Phys. Rev. Lett.*, 123(23):237207, 2019.

Acknowledgments

The authors thank Konrad Ferdinand Scharff, Markus Garst, Jörg Schmalian and Haifeng Ding for helpful discussions. This work was funded by the Deutsche Forschungsgemeinschaft (DFG) in the framework of TRR 288-422213477 (Project B06 and B03), CRC 1238-277146847 (Project C01) and the Cluster of Excellence Matter and Light for Quantum Computing (ML4Q) EXC 2004/1-390534769.

Author contributions

N.B., Q.L. and P.N. performed the STM measurements supervised by W.W.. L.Z. and Y.M. conducted the first-principles calculations for phonons. Q.L., W.W. and Y.M developed the model calculations. A.H. grew the single crystal sample Fe_3GeTe_2. C.S. performed the electrical resistivity measurements. Q.L., N.B. and W.W. wrote the manuscript with the inputs from all co-authors.

Competing interests

The authors declare no conflict of interest.

Additional information

Supplementary information The online version contains supplementary material available at URL.